Mapping Local Charge Recombination Heterogeneity by Multidimensional Nanospectroscopic Imaging

Wei Bao *et al.*

Science **338**, 1317 (2012);
DOI: 10.1126/science.1227977

periods in ~6 billion years. Indeed, their scenario produces a good match to the $m_c \sim 0.01\ M_\odot$, $P_{orb} \sim 0.065$ days seen for PSR J1311−3430. At this point in the evolution the system is detached, the companion is He-dominated, and irradiation has taken over the evolution. Presumably, continued irradiation can drive the system toward PSR J1719−1438-type companion masses, or produce an isolated MSP.

The direct detection of an MSP in a blind search of gamma-ray data implies that further MSPs, including other extreme binary pulsars, may exist among the bright, as yet unidentified 2FGL gamma-ray sources [e.g., (*34*, *35*)], which are too radio-faint or obscured by dense companion winds to be found in typical radio searches.

References and Notes

1. D. C. Backer, S. R. Kulkarni, C. Heiles, M. M. Davis, W. M. Goss, *Nature* **300**, 615 (1982).
2. W. B. Atwood *et al.*, *Astrophys. J.* **697**, 1071 (2009).
3. A. A. Abdo *et al.*, *Science* **325**, 848 (2009).
4. D. A. Smith *et al.*, *Astron. Astrophys.* **492**, 923 (2008).
5. The term "blind search" is used to reflect the fact that the pulsar parameters are unknown a priori, implying that a wide range of pulsar parameters must be explicitly searched.
6. A. A. Abdo *et al.*, *Science* **325**, 840 (2009).
7. P. M. Saz Parkinson *et al.*, *Astrophys. J.* **725**, 571 (2010).
8. H. J. Pletsch *et al.*, *Astrophys. J.* **744**, 105 (2012).
9. H. J. Pletsch *et al.*, *Astrophys. J.* **755**, L20 (2012).
10. P. S. Ray *et al.*, http://arxiv.org/abs/1205.3089 (2012).
11. K. P. Watters, R. W. Romani, *Astrophys. J.* **727**, 123 (2011).
12. J. W. T. Hessels *et al.*, *Science* **311**, 1901 (2006).
13. P. L. Nolan *et al.*, *Astrophys. J.* **199** (suppl.), 31 (2012).
14. C. E. Fichtel *et al.*, *Astrophys. J.* **94** (suppl.), 551 (1994).
15. R. W. Romani, *Astrophys. J.* **754**, L25 (2012).
16. A. S. Fruchter, D. R. Stinebring, J. H. Taylor, *Nature* **333**, 237 (1988).
17. P. R. Brady, T. Creighton, *Phys. Rev. D* **61**, 082001 (2000).
18. H. J. Pletsch, B. Allen, *Phys. Rev. Lett.* **103**, 181102 (2009).
19. H. J. Pletsch, *Phys. Rev. D* **82**, 042002 (2010).
20. H. J. Pletsch, *Phys. Rev. D* **83**, 122003 (2011).
21. W. B. Atwood, M. Ziegler, R. P. Johnson, B. M. Baughman, *Astrophys. J.* **652**, L49 (2006).
22. O. C. de Jager, B. C. Raubenheimer, J. W. H. Swanepoel, *Astron. Astrophys.* **221**, 180 (1989).
23. M. Kerr, *Astrophys. J.* **732**, 38 (2011).
24. C. Messenger, *Phys. Rev. D* **84**, 083003 (2011).
25. See supplementary materials on *Science* Online.
26. P. S. Ray *et al.*, *Astrophys. J.* **194** (suppl.), 17 (2011).
27. G. B. Hobbs, R. T. Edwards, R. N. Manchester, *Mon. Not. R. Astron. Soc.* **369**, 655 (2006).
28. S. M. Ransom *et al.*, *Astrophys. J.* **727**, L16 (2011).
29. B. Paczyński, *Annu. Rev. Astron. Astrophys.* **9**, 183 (1971).
30. J. Frank, A. R. King, D. J. Raines, *Accretion Power in Astrophysics* (Cambridge Univ. Press, Cambridge, 1985).
31. M. Bailes *et al.*, *Science* **333**, 1717 (2011).
32. L. M. van Haaften, G. Nelemans, R. Voss, P. G. Jonker, *Astron. Astrophys.* **541**, A22 (2012).
33. O. G. Benvenuto, M. A. De Vito, J. E. Horvath, *Astrophys. J.* **753**, L33 (2012).
34. R. W. Romani, M. S. Shaw, *Astrophys. J.* **743**, L26 (2011).
35. M. Ackermann *et al.*, *Astrophys. J.* **753**, 83 (2012).

Acknowledgments: This work was supported by the Max-Planck-Gesellschaft. The Fermi LAT Collaboration acknowledges support from several agencies and institutes for both development and the operation of the LAT as well as scientific data analysis. These include NASA and Department of Energy (United States), CEA/Irfu and IN2P3/CNRS (France), ASI and INFN (Italy), MEXT, KEK, and JAXA (Japan), and the K. A. Wallenberg Foundation, the Swedish Research Council, and the National Space Board (Sweden). Additional support from INAF in Italy and CNES in France for science analysis during the operations phase is also gratefully acknowledged. Fermi LAT data are available from the Fermi Science Support Center (http://fermi.gsfc.nasa.gov/ssc).

Supplementary Materials

www.sciencemag.org/cgi/content/full/science.1229054/DC1
Materials and Methods
Figs. S1 and S2
References (*36*–*38*)

20 August 2012; accepted 17 October 2012
Published online 25 October 2012;
10.1126/science.1229054

Mapping Local Charge Recombination Heterogeneity by Multidimensional Nanospectroscopic Imaging

Wei Bao,[1,2]* M. Melli,[1]* N. Caselli,[3,4] F. Riboli,[3,4] D. S. Wiersma,[3,5] M. Staffaroni,[6] H. Choo,[7] D. F. Ogletree,[1] S. Aloni,[1] J. Bokor,[1,6] S. Cabrini,[1]† F. Intonti,[3,4] M. B. Salmeron,[1,2] E. Yablonovitch,[6] P. J. Schuck,[1]† A. Weber-Bargioni[1]†

As materials functionality becomes more dependent on local physical and electronic properties, the importance of optically probing matter with true nanoscale spatial resolution has increased. In this work, we mapped the influence of local trap states within individual nanowires on carrier recombination with deeply subwavelength resolution. This is achieved using multidimensional nanospectroscopic imaging based on a nano-optical device. Placed at the end of a scan probe, the device delivers optimal near-field properties, including highly efficient far-field to near-field coupling, ultralarge field enhancement, nearly background-free imaging, independence from sample requirements, and broadband operation. We performed ~40-nanometer–resolution hyperspectral imaging of indium phosphide nanowires via excitation and collection through the probes, revealing optoelectronic structure along individual nanowires that is not accessible with other methods.

In the study of materials, optical microscopy maps the spatial distribution of a specific quantity (such as morphology), whereas optical spectroscopy provides physical and chemical material properties (such as electronic structure). An ongoing challenge to understanding matter at the nanoscale is the difficulty in carrying out local optical spectroscopy. On a fundamental level, this should be possible by squeezing light beyond the diffraction limit (*1*–*4*). Optical antenna–based geometries have been designed to address this nanospectroscopy imaging problem by transforming light from the far field to the near field, but with limitations on sensitivity, bandwidth, resolution, and/or sample types (*5*).

We report a strategy that overcomes these limitations, based on a geometry that is capable of efficiently coupling far-field light to the near field and vice versa, without background illumination over a wide range of wavelengths. The geometry consists of a three-dimensional (3D) tapered structure terminating in a nanometer-sized gap (Fig. 1A), with a shape resembling that of a "campanile" bell tower (hereafter referred to as campanile). We demonstrated with the campanile probe hyperspectral imaging of local optoelectronic properties in indium phosphide nanowires (InP NWs) by exciting and collecting signal through the probe tip. InP NWs, with their direct solar spectrum–matched bandgap and presumed low surface recombination velocity, are expected to be the central functional elements of next-generation light-harvesting devices. With the campanile probe, we collect full spectra at each pixel in a scan image, revealing photoluminescence (PL) heterogeneity along individual NWs by mapping local charge recombination originating from trap states: critical optoelectronic information that was unobtainable with previous methods.

Various near-field probe geometries have been engineered with extraordinary optical transmission (*6*) or with coupled optical antenna structures (*7*, *8*) directly on the scanning-probe apex, greatly improving coupling efficiencies as compared to conventional aperture-based probes (*9*)

[1]Molecular Foundry, Lawrence Berkeley National Laboratory, Berkeley, CA 94720, USA. [2]Department of Materials Science and Engineering, University of California Berkeley, Berkeley, CA 94720, USA. [3]European Laboratory for Non-Linear Spectroscopy, 50019 Sesto Fiorentino, Firenze, Italy. [4]Dipartimento di Fisica e Astronomia, Università di Firenze, 50019 Sesto Fiorentino, Firenze, Italy. [5]Istituto Nazionale di Ottica (CNR-INO), 50125 Firenze, Italy. [6]Department of Electrical Engineering and Computer Sciences, University of California Berkeley, Berkeley, CA 94720–1770, USA. [7]Department of Electrical Engineering, California Institute of Technology, Pasadena, CA 91125, USA.

*These authors contributed equally to this work.
†To whom correspondence should be addressed. E-mail: afweber-bargioni@lbl.gov (A.W.-B.); scabrini@lbl.gov (S.C.); pjschuck@lbl.gov (P.J.S.)

(fig. S2). However, these rely on resonant structures with limited spectral bandwidth and have often used excitation modalities that are not background-free, in which a diffraction-limited (or larger) spot illuminates the optical antenna, but also excites portions of the sample not in the immediate vicinity of the tip, leading to unwanted background (*10*, *11*). Of note are recent approaches combining elements of apertureless near-field scanning optical microscopy (a-NSOM) tips with efficient photon-to-plasmon coupling structures that can be illuminated far from the sample (*11*, *12*). When designed correctly, these types of probes can be broadband because they exploit adiabatic plasmonic compression (*13*, *14*). There is, however, one primary drawback to these probes: A large enhancement is achieved only for very small tip/metallic-substrate gap modes. Therefore, only very thin samples (such as molecular monolayers) can be studied. Our work overcomes these problems, merging broadband field enhancement and confinement with efficient bidirectional coupling between far-field and near-field electromagnetic energy. We take advantage of the campanile concept to map optoelectronic properties of InP NWs.

The campanile probe is based on a 3D tapered metal-insulator-metal (MIM) structure ending in a nanogap (Fig. 1, A to C). Our simulations show that this geometry provides efficient coupling between far and near fields (Fig. 1D), because the fundamental mode in an MIM structure is supported without any cutoff frequency, no matter how thin the insulating layer (*13*). In the optical regime, where plasmonic effects become important at small length scales, it has been shown that efficient delivery of far-field light to a confined ultrasmall region is possible in two dimensions, using a tapered planar MIM structure [>70% conversion efficiency (*15*)], and in three dimensions with a dimple lens structure (*16*). The bidirectional coupling of the campanile probe is efficient over a large bandwidth (Fig. 1G), taking advantage of an adiabatically tapered (*13*, *14*) geometry used at longer wavelengths [such as the microwave and terahertz regimes (*17*)] to provide one of the simplest broadband methods for effectively overcoming the diffraction limit. The bandwidth is limited only by metal absorption at short wavelengths and can be extended well into the infrared region and beyond.

The plasmonic mode in the campanile is confined to the gap region, which thus defines the spatial resolution as well as the field enhancement [the ratio of electric field strength ($|E|$) in the gap to the incoming field strength ($|E_0|$)]. This ratio is greater than that from a bowtie antenna with the same-sized gap (Fig. 1G and fig. S1).

The highly confined field in the gap region avoids the illumination of large areas of the sample that is characteristic of other near-field methods: an important goal for nano-optical imaging and spectroscopy (*10*, *11*). Also, in the taper region, only a few photons leave the tip because of edge scattering and leakage before reaching the apex. Considering that we operate in a mode where signal is collected back through the antenna gap, the background from the sample arising from the edge-scattered light is insignificant and below the noise threshold in the PL images shown here. As with all near-field probes, the campanile tips interrogate only material located within a few nanometers of the apex (Fig. 1F), eliminating most background spectroscopic signal arising from bulk material or surrounding fluid.

Using standard nanofabrication techniques, the antenna design illustrated in Fig. 1A can be integrated into the apex of a number of scanning probes such as the cantilevers used in atomic force microscopy or into the tapered optical fibers used in conventional aperture-based NSOM. Representative images of a campanile tip used in this work are shown in Fig. 1, B and C. For a linearly tapered 3D MIM structure, the optimal taper angle is around 20° to 40°, over which range the transfer efficiency shows only minor changes (*13*). Similar properties could be obtained in a tapered cylindrical coaxial structure.

To demonstrate the utility of this concept, campanile tips with ~40-nm-wide gaps were used

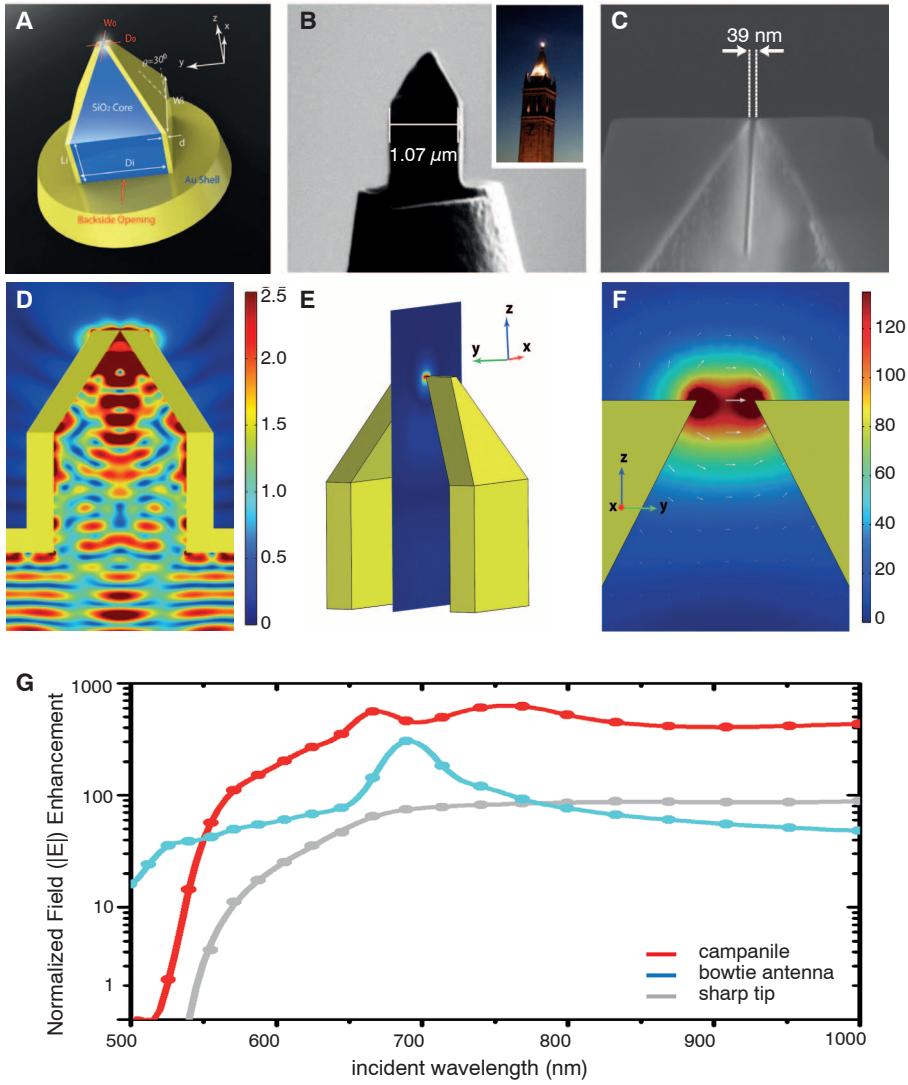

Fig. 1. Structure and optical properties of the 3D tapered (campanile) far-field to near-field transformer. The campanile geometry (**A**) is composed of a tapered metal insulator–metal waveguide fabricated at the end of a tapered glass fiber (**B**) by focused ion beam milling. Its shape resembles that of a bell tower of the same name (inset: photo of the Berkeley campanile), with a 39-nm (±2 nm) gap between the 3D tapered Au plates (**C**). (**D**) Finite element simulations reveal the highly efficient bidirectional coupling between macro and nano length scales (the electric field strength color-scale contrast is saturated to show the much weaker photonic and weakly confined plasmonic modes). Extending the contrast over the full color scale shows the nearly background-free near-field enhancement at the tip apex (**E**), while maintaining the linear polarization of the far field (**F**) (gap size = 10 nm; wavelength = 666 nm). (**G**) The ultralarge field ($|E|$) enhancement for a campanile with a 2-nm gap extends over larger bandwidth (red curve) than does a coupled optical bowtie antenna (blue curve) with a 2-nm gap or a sharp Au tip with a 20-nm radius of curvature (gray curve; assuming 100% light-coupling efficiency to the Au tip).

to map out the inhomogeneous radiative recombination in individual InP NWs, chosen because of their PL emission properties and potential as an ideal nanomaterial for light-harvesting due to the 1.4-eV bandgap and presumed low surface recombination rates (*18*–*20*). Trap states are believed to be responsible for many optical phenomena in nanocrystals and wires (*21*, *22*), including surface state–mediated luminescence modification in InP NWs (*23*), but are not well understood because of optical resolution limitations. Gaining this crucial insight requires both local optical excitation and local luminescence collection.

The glass fiber with the campanile tip was mounted in a shear-force scanner and coupled to a 633-nm laser. The near-field spot was scanned over the sample to locally excite and collect PL from InP NWs. Because of the huge field enhancement, only 100 μW of pre–fiber-coupled laser excitation power was needed to obtain a full emission spectrum between 760 and 900 nm. With a 100-ms integration time, a signal-to-noise ratio >60/1 was achieved.

Topography and a full spectrum were recorded at each image pixel, and PL maps were built by taking slices from the hyperspectral data set, which contains both amplitude and spectral variations. Figure 2 shows a 95-nm-wide InP NW imaged with a scanning electron microscope (Fig. 2A), with the campanile tip (Fig. 2B) and with a far-field confocal microscope (Fig. 2C). The confocal excitation power was the same as that used with the campanile tip. As can be seen, the campanile tip provides an optical resolution approximately equal to the gap size and much higher than the confocal resolution (Fig. 2D), as shown in the line scans in Fig. 2E, taken along the NW.

A typical PL spectrum from the center of a wire is shown in Fig. 3A, with the band-edge emission peak at 839 nm (1.47 eV) corresponding to the expected 100-meV blueshift relative to bulk InP NWs, independent of quantum confinement (*23*). Moreover, we observe various shoulders 40 to 100 meV above the band-edge emission that broaden the spectra considerably. With the campanile tip, we observed the spectral intensity and linewidth variations along individual NWs. PL emission intensities along the wire are mapped in Fig. 3, B to F, for wavelengths of 783, 802, 821, 839, and 857 nm. The first three maps represent the different shoulders above the band-edge emission and display considerable (300%) local variation of the PL intensity along an individual wire. For energies less than or equal to the band edge, the PL intensity remains fairly homogenous along the wire. In addition, for some of the studied wires, we observed PL hotspots located approximately 250 to 300 nm from one or both ends of the wire (compare Fig. 3, G and H, and fig. S1). The hot spots show spectral broadening toward the blue with additional luminescence 40 to 100 meV above the band edge, as seen in the waterfall plot of PL spectra from various points along the wire (Fig. 3I; PL peak intensity normalized to 1 for clarity). In contrast, confocal PL measurements of the same wire (Fig. 3J) also display two maxima but show no spectral variations along the NW (Fig. 3L), in agreement with previous confocal studies.

It was previously observed that strong PL enhancements and PL blueshifts result from passivated InP NW surfaces (*23*). This was attributed to Coulombic interactions between excitons and positively charged trap states on the NW surfaces (*21*). These studies proposed that trap states influence the optoelectronic properties of nanocrystals and NWs much more strongly than commonly assumed. The exciton diffusion length in these materials is hundreds of nanometers, and therefore individual trap states within the diffusion volume should strongly influence the local absorption energy and charge recombination rate.

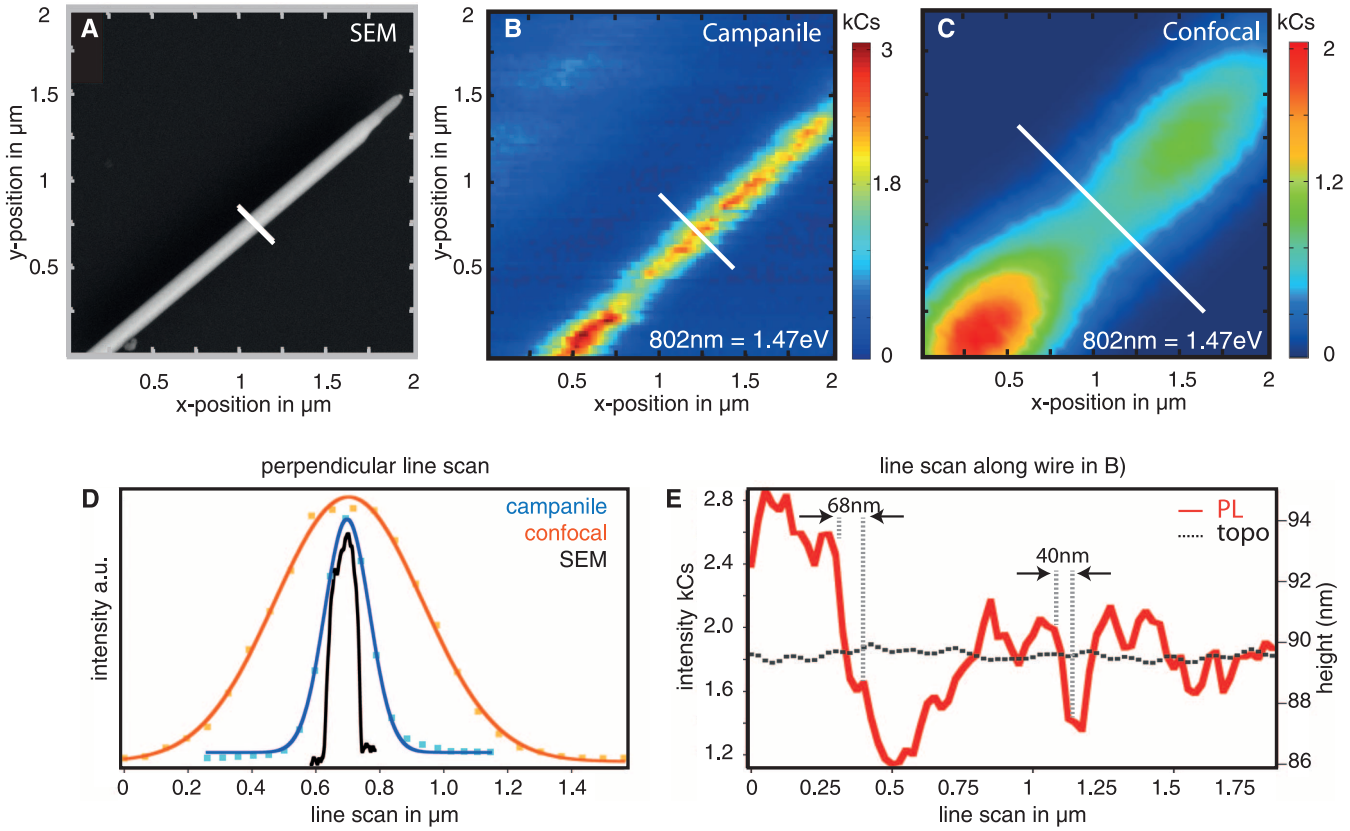

Fig. 2. Nano-optical hyperspectral PL mapping of InP NWs. (**A**) Scanning electron microscope (SEM) image of an InP NW that was hyperspectrally mapped with the campanile tip (**B**) (100 μW of excitation power, 100 ms per spectrum, map at 802 nm, intensity in kilocounts (kCs)), and confocally (**C**) (900 μW, 10 ms per spectrum, map at 802 nm). The near-field map (B) has considerably higher spatial resolution than the confocal map, as shown by the line scans across the wire (**D**) and strong local PL variations along the wire. a.u., arbitrary units. (**E**) A line scan along the wire length in (B) reveals a spatial resolution of ~40 nm (approximately equal to the gap size), whereas the topographic (topo) line scan shows negligible variations.

We believe that the heterogeneity observed along the wires (Figs. 2B and 3, B to F), on length scales well below the exciton diffusion length, are direct maps of trap-state modifications of the local exciton properties (*22*). The observed PL intensity hot spots (Fig. 3, G and J, and fig. S3) are probably due to an increase of trap-state densities (and changes in the native oxide layer) at the wire ends, resulting from the NW broken-end morphology. Their spectral characteristics are consistent with a trap-induced Stark shift, predicted to be ~60 to 70 meV above the band edge (*21*) for positive trap states (*23*), in accordance with our observations. Additionally, local trap states are known to cause Fermi level pinning and local band-bending in some cases (*21*), which would also affect local recombination rates. The absence of spectral variations in the confocal measurements is attributed to (i) lack of spatial resolution, and (ii) far-field PL measurement probing the entire NW thickness; i.e., surface-specific effects are obscured by bulk behavior. Cathodoluminescence measurements on InP NWs achieve a comparable resolution and provide complementary

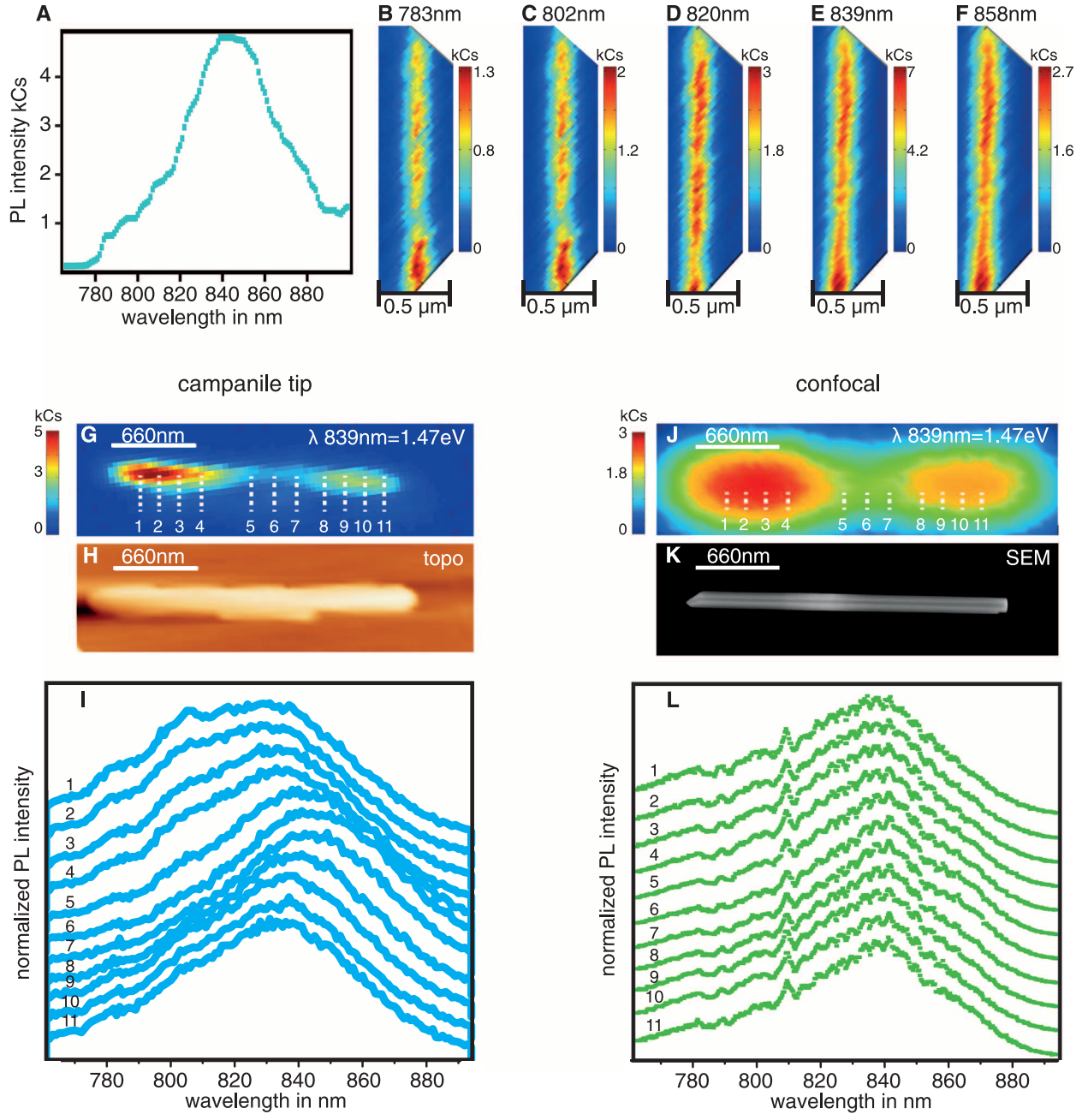

Fig. 3. Hyperspectral PL maps of InP NWs displaying local intensity (measured in kCs) and spectral variations. (**A**) Representative PL spectrum of the InP NW from Fig. 2, integrated over 10 ms. Various shoulders 40 to 100 nm above the band-edge emission at 839 nm are observed. Slices from the hyperspectral data at specific wavelengths are mapped (**B** to **F**), showing local intensity variations (up to a factor of 3) for the spectral components above the bandgap, whereas at bandgap energies and below, the PL is mostly homogenous. Images in (B) to (F) are raw data from a single hyperspectral scan. Other InP NWs displayed one (fig. S3) or two PL intensity hot spots (**G**) typically 250 to 300 nm from the wire ends as compared to topography (**H**) and SEM (**K**) images of the same NW. A waterfall plot of near-field spectra taken at positions 1 to 11 (peak emission intensity normalized to 1) shows strong local spectral variations, with the PL hot spots showing a band-edge blueshift as well as stronger contributions from trap-related spectral components above the bandgap (**I**). The same wire imaged confocally (**J**) displays two maxima but no spectral variations along the NW (**L**).

information. However, the large number of incident electrons fill the trap states and do not detect any spatial variation in emission from InP NWs (*24*).

We emphasize that the increased density of optical states at the tip apex will change the balance between various recombination pathways and may enable otherwise dark states to radiatively recombine (*25*–*27*). Finally, we note that measurements on NWs (and any sample thicker than ~2 nm) are not possible with NSOM in the tip-substrate gap mode, because that modality lacks the signal strength and sensitivity shown here, which is critical for investigating the majority of samples.

Campanile-style far-to-near–field transformers provide a pathway for understanding energy conversion processes at critical length scales, in our case yielding insights into the role of local trap states in radiative charge recombination in InP NWs. More generally, our study demonstrates the impact of the campanile geometry on a wide range of nano-optical measurements, because virtually all modes of optical imaging and spectroscopy are possible, including Raman and infrared/Fourier transform infrared hyperspectral imaging, as well as white-light nano-ellipsometry/interferometric mapping of dielectric functions. We expect that the combination of large bandwidth and enhancement makes them ideal for ultrafast pump-probe and/or nonlinear experiments down to molecular length scales (*28*–*31*). They also could be used for ultrasensitive medical detection, (photo) catalysis and quantum-optics investigations, as plasmonic optomechanics and circuitry elements, and as the cornerstone of tabletop high-harmonic/x-ray and photoemission sources.

References and Notes

1. R. Hillenbrand, T. Taubner, F. Keilmann, *Nature* **418**, 159 (2002).
2. L. Novotny, B. Hecht, *Principles of Nano-Optics* (Cambridge Univ. Press, Cambridge, 2006).
3. S. Kawata, Y. Inouye, P. Verma, *Nat. Photonics* **3**, 388 (2009).
4. D. Zhang *et al.*, *Phys. Rev. Lett.* **104**, 056601 (2010).
5. J. Stadler, T. Schmid, R. Zenobi, *Nanoscale* **4**, 1856 (2012).
6. Y. Wang, W. Srituravanich, C. Sun, X. Zhang, *Nano Lett.* **8**, 3041 (2008).
7. J. N. Farahani, D. W. Pohl, H. J. Eisler, B. Hecht, *Phys. Rev. Lett.* **95**, 017402 (2005).
8. A. Weber-Bargioni *et al.*, *Nano Lett.* **11**, 1201 (2011).
9. P. D. Yang *et al.*, *Adv. Funct. Mater.* **12**, 323 (2002).
10. D. Roy, J. Wang, C. Williams, *J. Appl. Phys.* **105**, 013530 (2009).
11. C. C. Neacsu *et al.*, *Nano Lett.* **10**, 592 (2010).
12. F. De Angelis *et al.*, *Nat. Nanotechnol.* **5**, 67 (2010).
13. M. Staffaroni, J. Conway, S. Vedantam, J. Tang, E. Yablonovitch, *Photonics Nanostructures Fundam. Appl.* **10**, 166 (2012).
14. M. I. Stockman, *Phys. Rev. Lett.* **93**, 137404 (2004).
15. P. Ginzburg, D. Arbel, M. Orenstein, *Opt. Lett.* **31**, 3288 (2006).
16. S. Vedantam *et al.*, *Nano Lett.* **9**, 3447 (2009).
17. E. Peytavit, J. F. Lampin, T. Akalin, L. Desplanque, *Electron. Lett.* **43**, 73 (2007).
18. J. F. Wang, M. S. Gudiksen, X. F. Duan, Y. Cui, C. M. Lieber, *Science* **293**, 1455 (2001).
19. J. M. Bao *et al.*, *Nano Lett.* **8**, 836 (2008).
20. K. Cho *et al.*, *Appl. Phys. Lett.* **98**, 203101 (2011).
21. A. Franceschetti, A. Zunger, *Phys. Rev. B* **62**, R16287 (2000).
22. S. A. Fischer, C. M. Isborn, O. V. Prezhdo, *Chem. Sci.* **2**, 400 (2011).
23. L. K. van Vugt, S. J. Veen, E. P. A. M. Bakkers, A. L. Roest, D. Vanmaekelbergh, *J. Am. Chem. Soc.* **127**, 12357 (2005).
24. N. Yamamoto, S. Bhunia, Y. Watanabe, *Appl. Phys. Lett.* **88**, 153106 (2006).
25. E. Shafran, B. D. Mangum, J. M. Gerton, *Phys. Rev. Lett.* **107**, 037403 (2011).
26. J. J. Greffet, *Science* **308**, 1561 (2005).
27. S. Kühn, U. Håkanson, L. Rogobete, V. Sandoghdar, *Phys. Rev. Lett.* **97**, 017402 (2006).
28. H. J. Maas *et al.*, *J. Opt. Soc. Am. B* **19**, 1295 (2002).
29. M. L. M. Balistreri, H. Gersen, J. P. Korterik, L. Kuipers, N. F. van Hulst, *Science* **294**, 1080 (2001).
30. P. Vasa, C. Ropers, R. Pomraenke, C. Lienau, *Laser Photon. Rev.* **3**, 483 (2009).
31. M. Seo *et al.*, *Nano Lett.* **10**, 2064 (2010).

Acknowledgments: The authors specifically thank E. Wong for fast and high-quality technical support, as well as our colleagues at the Molecular Foundry for stimulating discussion and assistance. We thank O. Yaghi, D. Milliron, M. Crommie, J. DeYoreo, and Y. D. Suh for valuable advice, discussions and reading of the manuscript. A provisional patent application regarding the fabrication of campanile-like structures on scan probes has been filed. Work at the Molecular Foundry was supported by the U.S. Department of Energy (DOE), Office of Basic Energy Sciences, Scientific User Facilities Division, under contract no. DE-AC02-05CH11231. Campanile tips were prepared by M. Melli, who was supported by the DOE, Office of Basic Energy Sciences, Materials Sciences and Engineering Division, under contract no. DE-AC02-05CH11231.

Supplementary Materials

www.sciencemag.org/cgi/content/full/338/6112/1317/DC1
Materials and Methods
Supplementary Text
Figs. S1 to S3
References (*32*, *33*)

26 July 2012; accepted 19 October 2012
10.1126/science.1227977

Robust Photogeneration of H_2 in Water Using Semiconductor Nanocrystals and a Nickel Catalyst

Zhiji Han,* Fen Qiu,* Richard Eisenberg,† Patrick L. Holland,† Todd D. Krauss†

Homogeneous systems for light-driven reduction of protons to H_2 typically suffer from short lifetimes because of decomposition of the light-absorbing molecule. We report a robust and highly active system for solar hydrogen generation in water that uses CdSe nanocrystals capped with dihydrolipoic acid (DHLA) as the light absorber and a soluble Ni^{2+}-DHLA catalyst for proton reduction with ascorbic acid as an electron donor at pH = 4.5, which gives >600,000 turnovers. Under appropriate conditions, the precious-metal–free system has undiminished activity for at least 360 hours under illumination at 520 nanometers and achieves quantum yields in water of over 36%.

Molecular hydrogen (H_2) is a clean-burning fuel that can be produced from protons (H^+) in the reductive half-reaction of artificial photosynthesis systems (*1*, *2*). One of the most prominent strategies for light-driven proton reduction features a multicomponent solution with a light-absorbing molecule (chromophore) that transfers electrons to a catalyst that reduces protons (*3*, *4*). However, these solution systems often use nonaqueous solvents and always have short lifetimes from decomposition of the chromophore over a period of hours (*5*). This difficulty has led to more-complicated architectures that separate the sites of light absorption and proton reduction (*2*).

Semiconductor nanocrystals (NCs) are promising alternative chromophores for light-driven proton reduction (*6*, *7*). Compared with traditional organic or organometallic chromophores, NCs have superior photostability, larger absorption cross-sections over a broad spectral range, orders of magnitude longer excited state lifetimes, electronic states and associated optical properties that vary with NC size, and the capacity to deliver multiple electrons with minimal structural perturbations (*6*, *7*). Heterostructures combining NCs with traditional precious-metal nanoparticle proton-reduction catalysts, or with iron hydrogenases, have produced efficient proton-reduction catalysis in solution (*8*–*10*). However, small-molecule catalysts in conjunction with NCs have given only modest H_2 production (*11*, *12*).

We report here a system that provides light-driven H_2 production with exceptional longevity, maintaining its high activity with no decrease for over 2 weeks using water as solvent. The system uses no precious metals and is based on light absorption and photoinduced electron transfer from semiconductor nanocrystals that are photochemically stable. Under optimal conditions, the system generates over 600,000 turnovers of H_2 (with respect to catalyst) without deterioration

Department of Chemistry, University of Rochester, Rochester, NY 14627, USA.

*These authors contributed equally to this work.
†To whom correspondence should be addressed. E-mail: eisenberg@chem.rochester.edu (R.E.); holland@chem.rochester.edu (P.L.H.); krauss@chem.rochester.edu (T.D.K.)